SCIENCE CHINA
Technological Sciences

•Article•

December 2022 Vol.65 No.12: 3020–3028
https://doi.org/10.1007/s11431-022-2192-6

Anchoring Pt nanoparticles and $Ti_3C_2T_x$ MXene nanosheets on CdS nanospheres as efficient synergistic photocatalysts for hydrogen evolution

JIANG JiZhou[1], XIONG ZhiGuo[1], WANG HaiTao[1*], XIANG Kun[1], WU PingXiu[2] & ZOU Jing[1*]

[1] *School of Environmental Ecology and Biological Engineering, School of Chemistry and Environmental Engineering, Key Laboratory of Green Chemical Engineering Process of Ministry of Education, Engineering Research Center of Phosphorus Resources Development and Utilization of Ministry of Education, Novel Catalytic Materials of Hubei Engineering Research Center, Wuhan Institute of Technology, Wuhan 430205, China;*

[2] *Semiconductor Electronic Special Gas of Hubei Engineering Research Center, Jingzhou 434000, China*

Received June 20, 2022; accepted August 22, 2022; published online November 18, 2022

The development of a new-fashioned functional nanomaterial with an outstanding photocatalytic hydrogen evolution reaction (HER) activity under visible-light irradiation is a sustainable and promising strategy to cope with the increasingly serious global energy crisis. Herein, an advanced ternary photocatalytic HER catalyst, in which the Pt nanoparticles and $Ti_3C_2T_x$ nanosheets are synchronously anchored on the surface of CdS nanospheres ($Ti_3C_2T_x$/Pt@CdS), is elaborately constructed via acid etching, self-reduction, and solvothermal treatment. Therein, the synergistic promoting effect between $Ti_3C_2T_x$ and Pt on the charge transfer of CdS effectively hinders the backtransfer of electrons to recombine with holes, resulting in a high-effective utilization of photo-excited charges. The obtained $Ti_3C_2T_x$/Pt@CdS possesses a superior photocatalytic HER activity compared to that of single active component catalyst. This work demonstrates the great potential of MXene materials in constructing high performance photocatalysts.

Pt nanoparticles, $Ti_3C_2T_x$ MXene, CdS nanospheres, synergistic catalytic effect, photocatalytic HER

Citation: Jiang J Z, Xiong Z G, Wang H T, et al. Anchoring Pt nanoparticles and $Ti_3C_2T_x$ MXene nanosheets on CdS nanospheres as efficient synergistic photocatalysts for hydrogen evolution. Sci China Tech Sci, 2022, 65: 3020–3028, https://doi.org/10.1007/s11431-022-2192-6

1 Introduction

Due to its inexhaustible and renewable advantages, solar energy is regarded as a promising alternative to fossil fuels under the severe situation of environmental pollution and resource shortage [1]. Among possible approaches, the HER via photocatalytic water splitting is one of the most promising technologies to convert solar energy into chemical energy [2–4]. Unfortunately, its sluggish kinetics severely restricts the widespread employment of photocatalytic water splitting [5]. In the past decade, researchers are devoted to developing efficient and stable HER catalysts, including precious metal supported composites, transition metal compounds, and metal-free nanomaterials [6–9]. Among these, CdS is considered as an attractive photocatalyst due to its beneficial characteristics of excellent visible-light absorption capacity and favorable conduction band positions for H_2 reducing [10–12]. Nevertheless, the constitutive photocatalytic activity of pristine CdS is still limited by the inherent defects of insufficient surface-active sites and rapid charge recombination [13,14]. In this regard, intensive efforts have been devoted to consolidating the photocatalytic

*Corresponding authors (email: wanghaitao@wit.edu.cn; jingzou@wit.edu.cn)

HER performance of CdS, including heterostructure construction, heteroatoms doping, morphology modulation and defect engineering [15–18]. Therein, coupling of precious metal nanoparticles (Au, Ag, Pt, etc.) with CdS to form heterojunctions is one of the most representative strategies for promoting catalytic activity [19–21]. Compared with single-ingredient CdS, the precious metal-included multi-component heterojunctions not only facilitate the electron separation efficiency of CdS arising from the low Fermi energy level and excellent electron capture ability of noble metal but also supply more proton reduction sites for HER, thereby obtaining superior photocatalytic activity [22]. For instance, Ma et al. [23] and Yu et al. [24] significantly enhanced the photocatalytic HER activity of CdS through coupling it with Au nanoparticles. Luo et al. [25] confirmed that the deposition of specific-shaped Pt nanoparticles on CdS significantly promoted its photocatalytic performance. Multi-metal hybrid CdS-based photocatalysts that combine dual precious metal were also reported, recently. For example, Ma et al. [26] mingled Au nanotriangles and Pt nanoparticles with CdS to construct a multi-metal hetero-nanostructure. Compared with pure CdS, these hetero-nanostructures displayed an appreciable enhancement in HER rate. However, most of the precious metal-included CdS catalysts currently developed cannot meet the requirements of commercial applications due to the high cost caused by the large dosage of noble metal. Seeking highly-active and low-cost substitutes to reduce the employment of precious metals is of paramount significance for constructing high performance CdS-based multicomponent photocatalysts.

As a new 2D transition-metal carbides, nitrides, and carbonitrides, MXene have attracted intensive interest in the fields of energy storage and conversion, due to their good hydrophilic ability, high electrical conductivity, and appropriate work function [27–29]. Moreover, a recent research confirmed that the Fermi level of $Ti_3C_2T_x$ is much lower than that of CdS [30]. Predictably, after coupling of CdS with $Ti_3C_2T_x$, electrons will be enriched on the surface of the latter [31]. Such a directional electron transfer between CdS and $Ti_3C_2T_x$ is expected to significantly inhibit the recombination of the electron and hole pairs of CdS [32]. In addition, since the surface of MXene, especially that of $Ti_3C_2T_x$ (T denotes -OH, -F, or -O-), has abundant hydrophilic functionalities, it can connect easily with CdS [33,34]. However, available results for enhancing the photocatalytic activity of CdS through integrating with $Ti_3C_2T_x$ are still limited. Investigating the vital function of $Ti_3C_2T_x$ on the photocatalytic performance of CdS is important, although remains challenging.

Considering the above viewpoints, let us focus herein a novel and efficient ternary photocatalyst, in which active $Ti_3C_2T_x$ MXene nanosheets and Pt nanoparticles are anchored uniformly on the surface of CdS nanospheres. In photocatalytic HER, the electrons of $Ti_3C_2T_x$/Pt@CdS tend to transfer from CdS to $Ti_3C_2T_x$, and eventually concentrate on Pt. This arises from the difference in the Fermi levels between its components, which accelerate the separation of photo-generated carriers effectively. Benefiting from this synergistic promoting effect between $Ti_3C_2T_x$ and Pt on the charge transfer of CdS, the ternary $Ti_3C_2T_x$/Pt@CdS sample demonstrates a much better photocatalytic HER rate under visible-light irradiation than Pt@CdS and $Ti_3C_2T_x$/CdS. In addition to providing a promising MXene-based photocatalyst, this work also proposes an instructive paradigm for further rational construct efficient multi-component catalysts, which is of practical significance.

2 Experimental procedure

2.1 Synthesis of $Ti_3C_2T_x$

$Ti_3C_2T_x$ MXene nanosheets were synthesized by a LiF-HCl etching method, where 1.6 g of LiF was introduced to 20 mL of 12 mol L^{-1} HCl and fully mixed at 25°C for 0.5 h. Then, 1 g of commercial Ti_3AlC_2 powder was added in the above solution under continuous stirring at 40°C for 48 h to etch its Al layer. After water washing, centrifuging (at 3500 r min^{-1}), and freeze drying, black solid powders named as $Ti_3C_2T_x$ were obtained, where T_x represents the termination functional groups on its surface, such as –OH and –F.

2.2 Fabrication of $Ti_3C_2T_x$/Pt

$Ti_3C_2T_x$/Pt catalyst was prepared by a self-reduction method. Briefly, 50 mg of $Ti_3C_2T_x$ powders and 4 mL of $H_2PtCl_6{\cdot}6H_2O$ solution (2.5 mg mL^{-1}) were introduced in 50 mL of ultrapure water with continuous stirring in a N_2 atmosphere for 0.5 h. $Ti_3C_2T_x$/Pt was then obtained after water washing, centrifugation (3500 r min^{-1}), and freeze drying treatments.

2.3 Preparation of CdS, Pt@CdS, $Ti_3C_2T_x$/CdS and $Ti_3C_2T_x$/Pt@CdS

$Ti_3C_2T_x$/Pt@CdS nanomaterials were fabricated by a solvothermal treatment, where 0.85 g of $Cd(CH_3COO)_2{\cdot}2H_2O$ and 4.84 mg of $Ti_3C_2T_x$/Pt were introduced in 60 mL of dimethyl sulfoxide (DMSO) under continuous stirring at 25°C for 1.5 h to form a uniform liquid mixture. The obtained solution was poured into a Teflon-lined autoclave and heated at 180°C for 12 h. After cooling naturally, $Ti_3C_2T_x$/Pt@CdS catalyst was obtained by washing and vacuum drying. For comparison, CdS samples were synthesized in a similar way just without the addition of $Ti_3C_2T_x$/Pt. Pt-free catalyst ($Ti_3C_2T_x$@CdS) was also fabricated through a similar way by replacing $Ti_3C_2T_x$/Pt with $Ti_3C_2T_x$, and $Ti_3C_2T_x$-free material (Pt@CdS) was prepared by introducing 2.50 mL of

$H_2PtCl_6·6H_2O$ (4.0 mg mL^{-1}) during the solvothermal synthesis of pure CdS.

3 Results and discussion

As schematically illustrated in Figure 1, the meticulous fabrication route of $Ti_3C_2T_x$/Pt@CdS is skillfully realized via acid etching, self-reduction, and solvothermal treatment. A common acid etching process of commercial Ti_3AlC_2 powder is applied first, yielding a surface functional groups riched $Ti_3C_2T_x$ MXene. $Ti_3C_2T_x$/Pt composite is then synthesized by a dropwise addition of a certain amount of $H_2PtCl_6·6H_2O$ in $Ti_3C_2T_x$ suspension. This takes advantage of the strong reducibility of $Ti_3C_2T_x$, which benefits from the abundant terminated functional groups (e.g., –OH and –F) on its surface. Finally, $Ti_3C_2T_x$/Pt@CdS catalyst is prepared by a solvothermal treatment of $Cd(CH_3COO)_2·2H_2O$ in DMSO with trace $Ti_3C_2T_x$/Pt, in which $Cd(CH_3COO)_2·2H_2O$ and DMSO are employed as Cd and S sources, respectively.

The surface morphology of $Ti_3C_2T_x$/Pt@CdS is studied by field emission scanning electron microscopy (FESEM). The typical FESEM image displayed in Figure 1(a) discloses that the developed $Ti_3C_2T_x$/Pt@CdS catalyst possesses a well-defined spherical structure with an averaged diameter of ~500 nm. The corresponding enlarged FESEM images (Figure 2(b) and (c)) show that $Ti_3C_2T_x$/Pt@CdS has a rough surface, and a high-density of nanoparticles with a diameter smaller than 10 nm anchored on the spherical skeleton. To

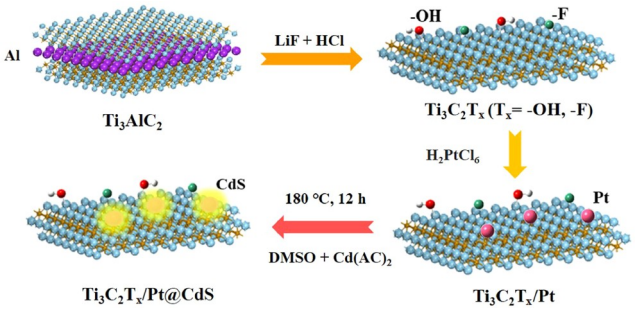

Figure 1 (Color online) Schematic illustration for the preparation of $Ti_3C_2T_x$/Pt@CdS.

know the composing elements of $Ti_3C_2T_x$/Pt@CdS and their distribution, an energy dispersive X-ray (EDX) analysis is first performed. Figure 2(d) exhibits the EDX patterns and the corresponding element mappings of $Ti_3C_2T_x$/Pt@CdS, where the salient elemental signals of C, Ti, and Pt demonstrate the successful integration of $Ti_3C_2T_x$ and Pt. Incorporating with the result of FESEM observation (Figure 2(c)), the uniform distribution of these elements confirms that $Ti_3C_2T_x$ and Pt nanoparticles are homogeneously dispersed on the surface of CdS nanospheres. The uniform size and excellent distribution of $Ti_3C_2T_x$ nanosheets and Pt nanoparticles on CdS nanospheres are anticipated to induce a positive effect on raising the photocatalytic activity of ternary composites.

The crystalline natures of the as-synthesized photocatalysts are investigated by the X-ray diffraction (XRD)

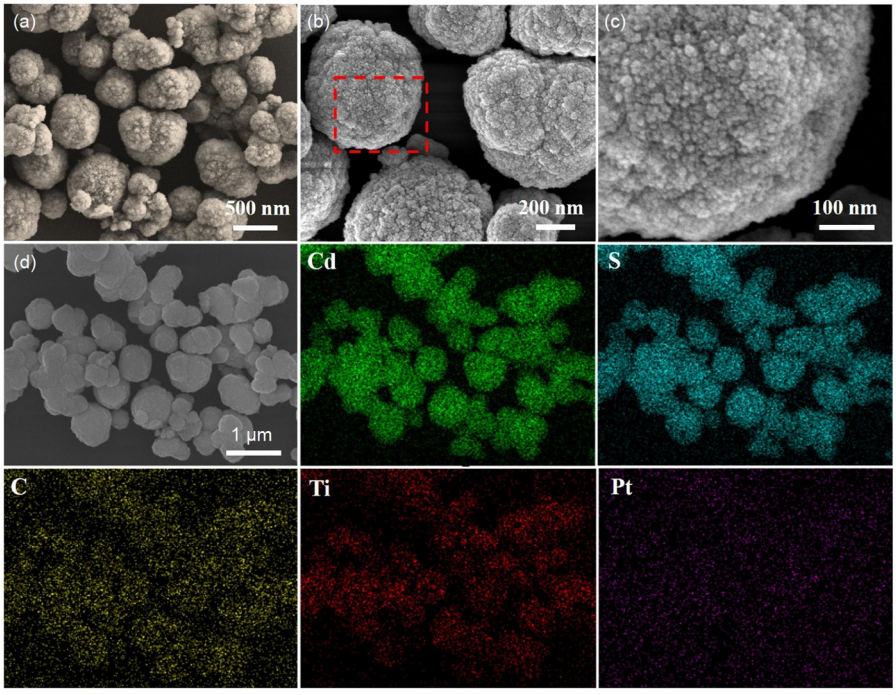

Figure 2 (Color online) (a)–(c) FESEM images of $Ti_3C_2T_x$/Pt@CdS. (d) Top-sectional view of FESEM image and the corresponding elemental mapping images of Cd, S, C, Ti, and Pt.

patterns shown in Figure 3(a), where three distinct peaks centered approximately at 26.6°, 44.6°, and 51.9° are observed. These correspond respectively to the (111), (220), and (311) diffraction planes of the hexagonal wurtzite-structured phase of CdS. It is worth noting that no diffraction peaks are observed for $Ti_3C_2T_x$ and Pt in Pt@CdS, $Ti_3C_2T_x$/CdS, and $Ti_3C_2T_x$/Pt@CdS. This may be attributed to the high dispersion and low loading of $Ti_3C_2T_x$ nanosheets and Pt nanoparticles on the surface of CdS. The undiscovered diffraction peak offset also proves the unchanged crystal structure of CdS after the introduction of $Ti_3C_2T_x$ and Pt. To illustrate the surface composition of $Ti_3C_2T_x$/Pt@CdS, X-ray photoelectron spectroscopy (XPS) measurements were carried out. Again, the full XPS survey spectrum displayed in Figure 3(b) reveals the presence of Cd, Pt, S, C, O, N, and Ti elements in $Ti_3C_2T_x$/Pt@CdS, which is consistent with the results of EDX (Figure 2(d)). Moreover, the tiny contents of Pt (0.26 at.%) and Ti (1.62 at.%) confirm the trace loading of $Ti_3C_2T_x$ and Pt on the surface of CdS (Table S1, Supplementary Information).

The influence of the integration of $Ti_3C_2T_x$ nanosheets and Pt nanoparticles on the surface area and textural porosity of CdS are analyzed by the N_2 adsorption-desorption isotherm and the corresponding Barrette-Joynere-Halenda (BJH) pore size distribution of CdS and $Ti_3C_2T_x$/Pt@CdS. As presented in Figure 3(c) and (d), the type II adsorption isotherm of $Ti_3C_2T_x$/Pt@CdS is accompanied by a remarkable hysteresis loop, indicating the coexistence of micropores and a mesoporous structure [35], which can also be verified by the corresponding pore size distributions (smaller than 55 nm) of $Ti_3C_2T_x$/Pt@CdS. Noteworthy, the surface area of $Ti_3C_2T_x$/Pt@CdS is estimated to be 19.01 $m^2 g^{-1}$, nearly two times that of CdS. This can be ascribed to the tiny particle size and the high dispersion of $Ti_3C_2T_x$ nanosheets and Pt nanoparticles on the surface of CdS. The increased specific surface area is anticipated to raise the number of surface active sites, thereby promoting the photocatalytic HER activity [36].

To further explore the chemical state of $Ti_3C_2T_x$/Pt@CdS, their high-resolution Cd 3d, S 2p, Ti 2p, C 1s, Pt 4f, and O 1s spectra are studied systematically, and the results obtained are illustrated in Figure 4 and Table S1. The Cd 3d and S 2p spectra of $Ti_3C_2T_x$/Pt@CdS show two peaks near 405.1 and 411.82 eV, which belong to the Cd $3d_{5/2}$ and Cd $3d_{3/2}$ of Cd^{2+} in CdS, respectively, while the signals located at 161.27 and 162.45 eV correspond to the S $2p_{3/2}$ and S $2p_{1/2}$ of S^{2-} of CdS, respectively [37]. The fitted Ti 2p spectra of $Ti_3C_2T_x$/Pt@CdS unveil six obvious peaks near 454.9, 457.0, 458.9, 461.1, 463.0, and 464.6 eV, correspond well to Ti-C $2p_{3/2}$, Ti-F, Ti-O $2p_{3/2}$, Ti-C $2p_{1/2}$, Ti-O_x $2p_{1/2}$, and Ti-O $2p_{1/2}$, respectively (Figure 4(c)) [38]. Therein, the appearance of Ti-O bond may arise from the surface oxidation of $Ti_3C_2T_x$ after contact with air, while the presence of Ti-F bond can be attributed to the formed –F terminations induced by LiF-HCl etching [39]. Figure S1 shows the high-resolution C 1s spectra of $Ti_3C_2T_x$/Pt@CdS, in which the peaks located at 284.84, 286.20, and 288.84 eV belong to C-C, C-O-C, and C-F, respectively [40,41], demonstrating again the successful

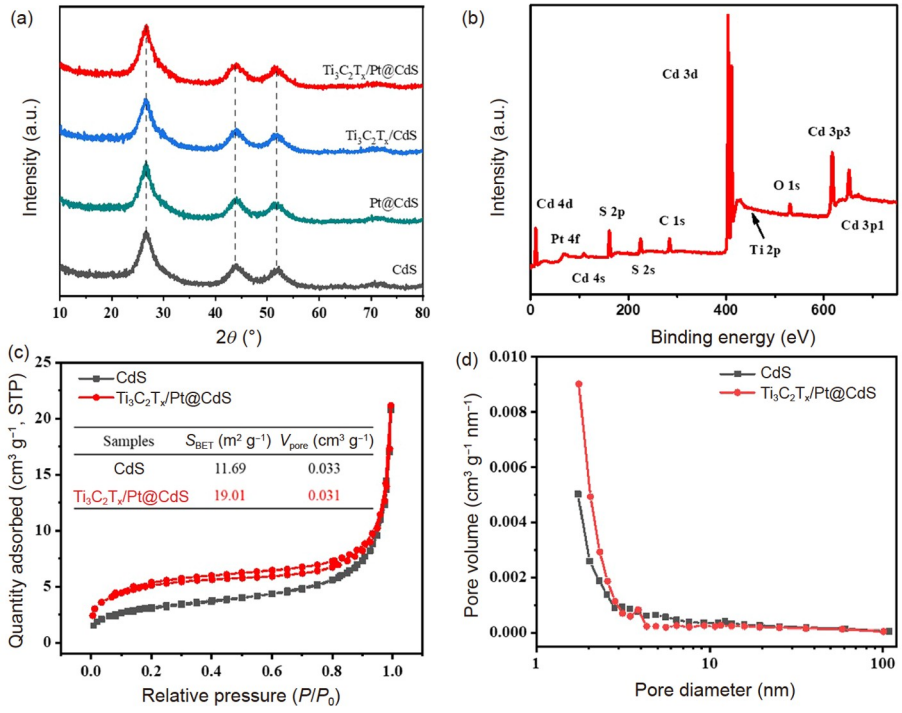

Figure 3 (Color online) (a) XRD patterns of CdS, Pt@CdS, $Ti_3C_2T_x$/CdS, and $Ti_3C_2T_x$/Pt@CdS. (b) XPS survey spectrum of $Ti_3C_2T_x$/Pt@CdS. (c) N_2 sorption isotherms, BET specific surface areas, total pore volumes and (d) the corresponding pore size distributions of CdS and $Ti_3C_2T_x$/Pt@CdS.

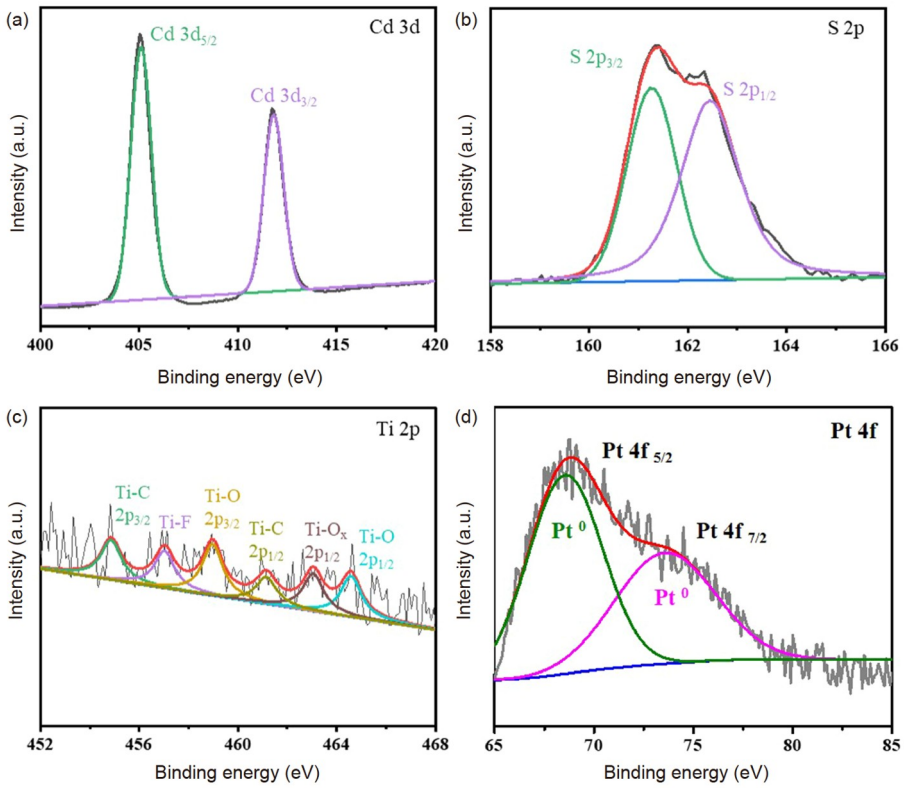

Figure 4 (Color online) High-resolution XPS spectra of (a) Cd 3d, (b) S 2p, (c) Ti 2p, and (d) Pt 4f of $Ti_3C_2T_x$/Pt@CdS.

generation of $Ti_3C_2T_x$ with abundant surface functionalities (-F and -O). The two distinct peaks centered at 68.59 and 73.81 eV in the high-resolution Pt 4f spectra displayed in Figure 4(d) correspond to the Pt $4f_{5/2}$ and Pt $4f_{7/2}$ of Pt^0, indicating the successful integration of Pt nanoparticles on CdS [42].

The photocatalytic HER performances of the as-obtained samples are examined in a triethanolamine aqueous solution under visible light (λ>420 nm) irradiation. Before that, the amount of $H_2PtCl_6{\cdot}6H_2O$ (4.0 mg mL^{-1}) and that of $Ti_3C_2T_x$/Pt added in the synthesis process are optimized first. Notably, superior photocatalytic HER activities are observed for Pt@CdS-2.5 mL and $Ti_3C_2T_x$/Pt@CdS-4.84 mg catalysts, indicating that the optimal addition of $H_2PtCl_6{\cdot}6H_2O$ and $Ti_3C_2T_x$/Pt are 2.5 mL and 4.84 mg, respectively (Figure S2). Therefore, the catalysts discussed below are fabricated at these optimal amounts of addition. In addition, due to the integration of $Ti_3C_2T_x$ and Pt, no co-catalyst is required in this work. Figure 5(a) illustrates the photocatalytic HER activities of all the materials examined. As expected, only a trace amount of H_2 is released in the case of pure CdS catalyst. In contrast, the photocatalytic HER activity is 552.9 μmol g^{-1} h^{-1} for the case of Pt@CdS, and 655.4 μmol g^{-1} h^{-1} for the case of $Ti_3C_2T_x$/CdS, which is 3.35 and 3.97 times that of bare CdS (164.9 μmol g^{-1} h^{-1}), respectively, highlighting the great potential of $Ti_3C_2T_x$ and Pt in promoting the photocatalytic HER efficiency of CdS. Surprisingly, if $Ti_3C_2T_x$ and Pt are introduced simultaneously, $Ti_3C_2T_x$/Pt@CdS yields a significant enhancement in HER rate (1401.8 μmol g^{-1} h^{-1}), which is about nine times that of pure CdS. This demonstrates the synergistic catalytic effect of $Ti_3C_2T_x$ and Pt in improving the photocatalytic HER activity of CdS. To the best of our knowledge, the developed $Ti_3C_2T_x$/Pt@CdS catalyst demonstrates one of the highest photocatalytic HER activities among other CdS or MXene-based photocatalysts (Table 1).

Figure 5(b) exhibits the apparent quantum efficiency (AQE) of $Ti_3C_2T_x$/Pt@CdS at different wavelengths, where the AQE values of 0.1% and 0.101% at 420 and 450 nm further confirm the excellent photocatalytic activity of $Ti_3C_2T_x$/Pt@CdS toward HER. The evaluated rates of photocatalytic HER of $Ti_3C_2T_x$/Pt@CdS at different visible light wavelengths are shown in Figure 5(c). Excitingly, the photocatalytic HER performance of $Ti_3C_2T_x$/Pt@CdS is also excellent in the ultraviolet region, indicating its versatile applications.

To explain the elevated photocatalytic activity of $Ti_3C_2T_x$/Pt@CdS ternary composites relative to that of pure CdS, we first examined the UV-vis diffuse reflectance spectroscopy of as-obtained photocatalysts. As exhibited in Figure 6(a), the characteristic absorption sharp edges of all the catalysts examined are located near 500 nm, which corresponds to the

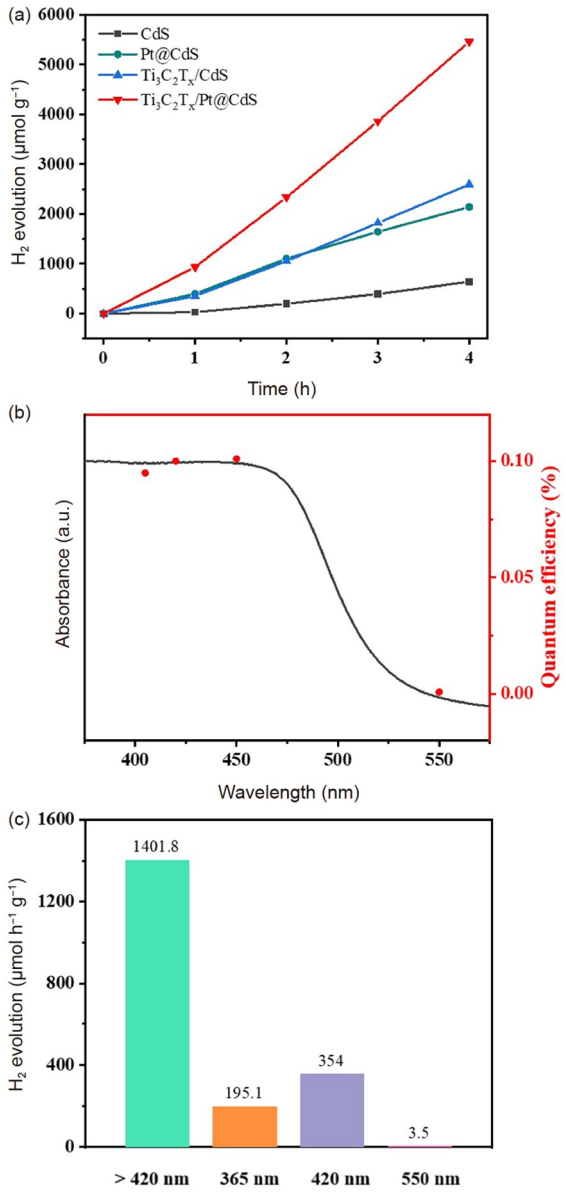

Figure 5 (Color online) (a) Photocatalytic HER activities of CdS, Pt@CdS, $Ti_3C_2T_x$/CdS, and $Ti_3C_2T_x$/Pt@CdS. (b) AQY of $Ti_3C_2T_x$/Pt@CdS. (c) Photocatalytic HER rate of $Ti_3C_2T_x$/Pt@CdS at various wavelengths.

intrinsic band-gap of CdS. This reveals that the light absorption of CdS is influenced insignificantly by the integration of $Ti_3C_2T_x$ and Pt. The Tauc plot corresponds to the UV-vis absorption spectra is presented in Figure S3, which reveals that the band gaps are 2.42, 2.43, and 2.42 eV for CdS, Pt@CdS, and $Ti_3C_2T_x$/CdS, respectively. To estimate the change in the band structure of CdS after integrating with $Ti_3C_2T_x$ and Pt, the Mott-Schottky (MS) plots of CdS, Pt@CdS, and $Ti_3C_2T_x$/CdS are recorded at different frequencies. The positive curvilinear incline slopes observed in Figures 6(b) and S3 suggest that CdS, Pt@CdS, and $Ti_3C_2T_x$/CdS are typical N-type semiconductor [50]. Therefore, the tested flat-band potentials can be represented approximately by the corresponding conduction band (CB) values [51]. Accordingly, the estimated CB potentials of CdS, Pt@CdS, and $Ti_3C_2T_x$/CdS are −0.68, −0.69, and −0.76 V (vs. RHE), respectively (Figures 6(b) and S4). Combined with the band gap value, the corresponding valence band (VB) potentials are 1.74, 1.74, and 1.66 V (vs. RHE) (Figure S5). Noticeably, the influence of introducing $Ti_3C_2T_x$ and Pt on the band structure alignment of CdS is inappreciable. Therefore, the light absorption capacity and band structure are not the primary cause for the superior photoactivity HER rate of $Ti_3C_2T_x$/Pt@CdS.

Transient photocurrent response (TPR) measurement is carried out to shed light on underlying charge separation efficiency. The TPR of CdS, Pt@CdS, $Ti_3C_2T_x$/CdS, and $Ti_3C_2T_x$/Pt@CdS are collected via an on-off visible-light illumination, and the results obtained are displayed in Figure 6(c). Compared with CdS, Pt@CdS, and $Ti_3C_2T_x$/CdS, $Ti_3C_2T_x$/Pt@CdS has the strongest photocurrent density, which demonstrates that the co-integration of $Ti_3C_2T_x$ and Pt can effectively boost the charge separation efficiency of CdS. The contribution of $Ti_3C_2T_x$ and Pt loading to the charge transfer behavior of CdS is explored by electrochemical impedance spectra (EIS) tests. As seen in Figure 6(d), the Nyquist semicircle is smallest for $Ti_3C_2T_x$/Pt@CdS, suggesting that the charge transfer between $Ti_3C_2T_x$/Pt@CdS and the electrolyte solution has the lowest resistance, and is fastest [52]. This is consistent with the results of linear sweeping voltammograms (LSVs) measurements presented in Figure 6(e). This figure reveals that $Ti_3C_2T_x$/Pt@CdS not only displays the smallest HER overpotential but also has the largest current density, similarly indicating that the most efficient charge transfer can be obtained by introducing $Ti_3C_2T_x$ and Pt on the surface of CdS. To further prove the favorable photo-generated carriers separation ability of CdS after integrating with $Ti_3C_2T_x$ and Pt, we examined the survival time (τ) of the photo-generated charge carriers via their transient fluorescence decay spectra. As shown in Figure 6(f) and Table S2, the averaged survival time (τ_{Avg}) of $Ti_3C_2T_x$/Pt@CdS is 7.580 ns, which is much longer than that of CdS (5.523 ns) and Pt@CdS (6.017 ns), revealing a significant positive effect of co-introducing $Ti_3C_2T_x$ and Pt in prolonging photo-generated carriers lifetime. The results gathered expound convincingly that the improved photo-generated carriers separation and migration rate result from the integration of $Ti_3C_2T_x$ and Pt are responsible for the high-efficiency photocatalytic HER activity of $Ti_3C_2T_x$/Pt@CdS.

On grounds of above analysis, a plausible charge-transfer pathway and the mechanism of ternary $Ti_3C_2T_x$/Pt@CdS for photocatalytic HER is proposed (Figure 7). As demonstrated previously that F-terminated MXene has a lower work function than CdS [53]. Moreover, the Fermi level (E_F) of $Ti_3C_2T_x$ is relatively high compared to that of Pt [54]. Therefore, to establish an E_F equilibrium after an intimate

Table 1 Comparison of the photocatalytic HER activities of $Ti_3C_2T_x$/Pt@CdS and those of other CdS or MXene-based photocatalysts previously reported

Catalysts	Loading (mg)	Light source (λ>420 nm)	Activities (μmol g^{-1} h^{-1})	Ref.
$Ti_3C_2T_x$/Pt@CdS	20	300 W Xe lamp	1401.8	This work
AuNR-CdS YSNs	3	300 W Xe lamp	563	[43]
Au-Pt-CdS	50	300 W Xe lamp	778	[26]
$Ti_3C_2T_x$/CdS	10	300 W Xe lamp	193.25	[32]
Ti/CdS-A2.5	50	300 W Xe lamp	1480	[44]
BVC3-T2	100	300 W Xe lamp	980	[45]
CT1	20	300 W Xe lamp	825	[46]
TM7-3	2.5	300 W Xe lamp	319.4	[47]
TS1.5	10	300 W Xe lamp	219.7	[31]
TiO_2/Ti_3C_2@AC-48h	3	350 W Xe lamp	33.4	[48]
CN/pTC3.0	50	350 W Xe lamp	17.8	[49]

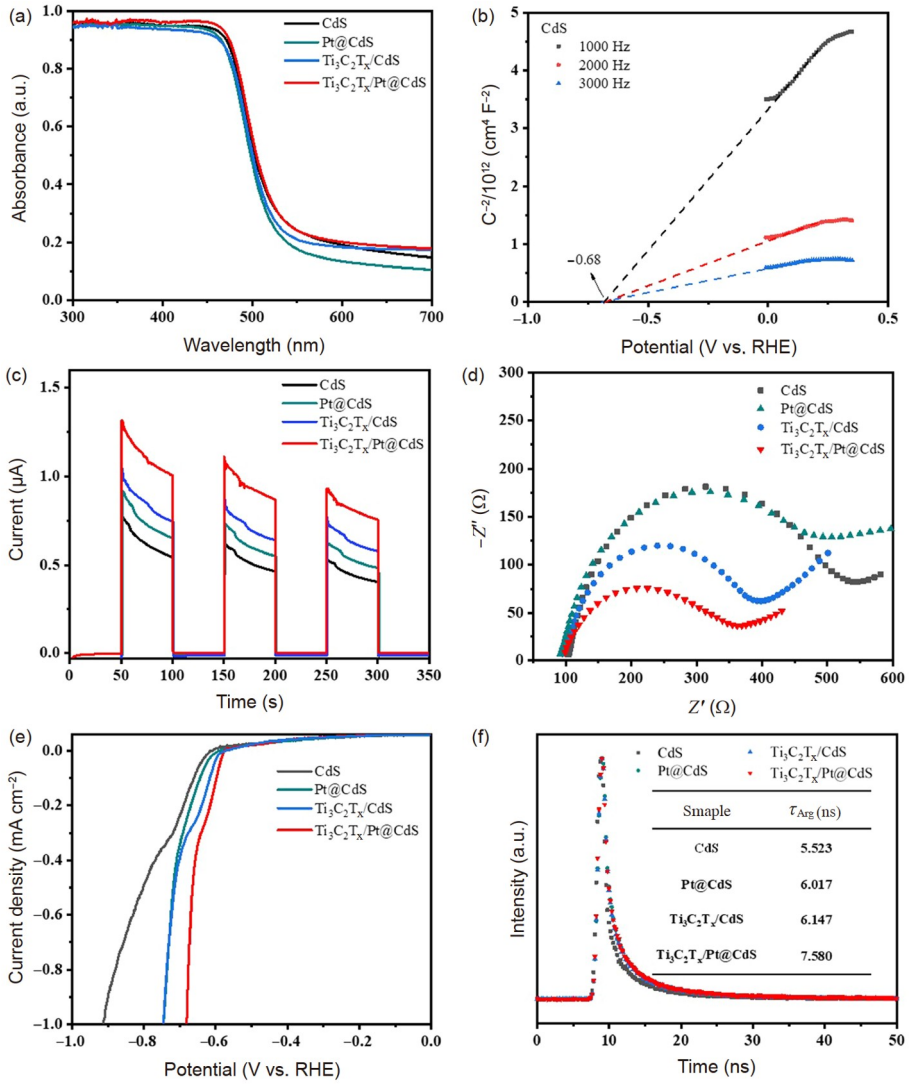

Figure 6 (Color online) (a) UV-vis absorption spectra of CdS, Pt@CdS, $Ti_3C_2T_x$/CdS, and $Ti_3C_2T_x$/Pt@CdS. (b) M-S plots of CdS at various frequencies. (c) TPR, (d) EIS plots, (e) LSVs, and (f) transient fluorescence decay spectra of CdS, Pt@CdS, $Ti_3C_2T_x$/CdS, and $Ti_3C_2T_x$/Pt@CdS.

contact, electrons tend to transfer from CdS to $Ti_3C_2T_x$, and eventually concentrate on Pt. As a result, the stepwise electron transfer from CdS to $Ti_3C_2T_x$ first, and then to Pt is implemented. It is worth mentioning that since Pt has the

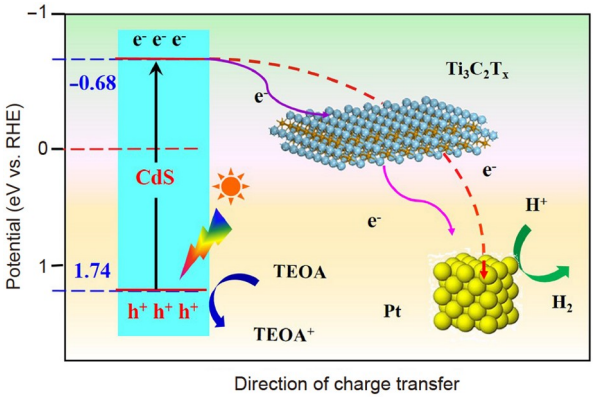

Figure 7 (Color online) Schematic diagram for the charge transfer in $Ti_3C_2T_x$/Pt@CdS during photocatalytic HER.

lowest E_F, the CB electrons of CdS coming from visible light excitation can also be directly transferred to Pt. Consequently, two charge transfer interfaces are constructed at the interface between CdS/$Ti_3C_2T_x$ and CdS/Pt, which effectively hinder the back transfer of electrons to recombine with holes, thereby resulting in a high-effective utilization of photo-generated carriers. Eventually, the photo-induced electrons accumulate on Pt and reduce the adsorbed H^+ to achieve photocatalytic HER. In other words, the synergistic catalytic effect between $Ti_3C_2T_x$ and Pt contributes to the significantly enhanced photocatalytic HER activity of CdS.

4 Conclusion

An advanced HER photocatalyst, in which Pt nanoparticles and $Ti_3C_2T_x$ MXene nanosheets are anchored on CdS nanospheres ($Ti_3C_2T_x$/Pt@CdS), has been explored successfully by acid etching of Ti_3AlC_2 followed by a self-reduction and solvothermal treatment. We demonstrate that a simultaneous integration of $Ti_3C_2T_x$ and Pt can improve the photocatalytic HER activity of CdS efficiently. In ternary $Ti_3C_2T_x$/Pt@CdS composites, due to the difference in the Fermi levels between single components, electrons tend to transfer from CdS to $Ti_3C_2T_x$, and eventually concentrated on Pt. This stepwise electron transfer can accelerate the separation of photo-generated carriers, resulting in a boosted utilization of electrons. Benefiting from the synergic catalytic effect between $Ti_3C_2T_x$ and Pt nanoparticles, $Ti_3C_2T_x$/Pt@CdS displays a significantly enhanced HER rate, which is much higher than that of $Ti_3C_2T_x$/CdS and Pt@CdS. We anticipate that the underlying stepwise electron-transfer mechanism confirmed in this study will open a new doorway to design efficient multicomponent catalysts.

This work was supported by the National Natural Science Foundation of China (Grant No. 62004143), the Key R&D Program of Hubei Province (Grant No. 2022BAA084), the Natural Science Foundation of Hubei Province (Grant No. 2021CFB133), and the Central Government Guided Local Science and Technology Development Special Fund Project (Grant No. 2020ZYYD033).

Supporting Information

The supporting information is available online at tech.scichina.com and link.springer.com. The supporting materials are published as submitted, without typesetting or editing. The responsibility for scientific accuracy and content remains entirely with the authors.

1 Nishiyama H, Yamada T, Nakabayashi M, et al. Photocatalytic solar hydrogen production from water on a 100-m^2 scale. Nature, 2021, 598: 304–307
2 Takata T, Jiang J, Sakata Y, et al. Photocatalytic water splitting with a quantum efficiency of almost unity. Nature, 2020, 581: 411–414
3 Wang S L, Xu Z J, Lin S, et al. Polymer-chlorella cells conjugating with aggregation-induced functionality switch towards hydrogen evolution. Sci China Tech Sci, 2020, 63: 1416–1425
4 Chen X, Wang J, Chai Y, et al. Efficient photocatalytic overall water splitting induced by the giant internal electric field of a g-C_3N_4/rGO/PDIP Z-scheme heterojunction. Adv Mater, 2021, 33: 2007479
5 Gao H M, Xiao M L, Li G Q, et al. Oxygen-vacancy-rich TiO_2 enables highly active and durable water electrolysis of urchin-like RuO_2 catalyst. Sci China Tech Sci, 2022, 65: 2317–2324
6 Jiang J, Xiong Z, Wang H, et al. Sulfur-doped g-C_3N_4/g-C_3N_4 isotype step-scheme heterojunction for photocatalytic H_2 evolution. J Mater Sci Tech, 2022, 118: 15–24
7 Zou J, Liao G, Jiang J, et al. *In-situ* construction of sulfur-doped g-C_3N_4/defective g-C_3N_4 isotype step-scheme heterojunction for boosting photocatalytic H_2 evolution. Chin J Struct Chem, 2022, 41: 2201025–2201033
8 Zhou Q, Liu H R, Jiao S Z, et al. Phosphorus-doped NiS_2 electrocatalyst with a hybrid structure for hydrogen evolution. Sci China Tech Sci, 2022, 65: 1506–1512
9 Jiang J, Li N, Zou J, et al. Synergistic additive-mediated CVD growth and chemical modification of 2D materials. Chem Soc Rev, 2019, 48: 4639–4654
10 Ge B, Ren G N, Zhao P F, et al. Preparation of superhydrophobic CdS cotton using visible light response and its application for the control of water pollution. Sci China Tech Sci, 2019, 62: 2236–2242
11 Xiong M, Yan J, Chai B, et al. Liquid exfoliating CdS and MoS_2 to construct 2D/2D MoS_2/CdS heterojunctions with significantly boosted photocatalytic H_2 evolution activity. J Mater Sci Tech, 2020, 56: 179–188
12 Wang W, Tao Y, Fan J, et al. Fullerene-graphene acceptor drives ultrafast carrier dynamics for sustainable CdS photocatalytic hydrogen evolution. Adv Funct Mater, 2022, 32: 2201357
13 Ding C, Zhao C, Cheng S, et al. Ultrahigh photocatalytic hydrogen evolution performance of coupled 1D CdS/1T-phase dominated 2D WS_2 nanoheterojunctions. Chin J Catal, 2022, 43: 403–409
14 Zhang L, Jiang X, Jin Z, et al. Spatially separated catalytic sites supplied with the CdS-MoS_2-In_2O_3 ternary dumbbell S-scheme heterojunction for enhanced photocatalytic hydrogen production. J Mater Chem A, 2022, 10: 10715–10728
15 Zhang E, Zhu Q, Huang J, et al. Visually resolving the direct Z-scheme heterojunction in CdS@$ZnIn_2S_4$ hollow cubes for photocatalytic evolution of H_2 and H_2O_2 from pure water. Appl Catal B-Environ, 2021, 293: 120213
16 Zubair M, Vanhaecke E M M, Svenum I H, et al. Core-shell particles of C-doped CdS and graphene: A noble metal-free approach for efficient photocatalytic H_2 generation. Green Energy Environ, 2020, 5: 461–472
17 Deng L, Fang N, Wu S, et al. Uniform H-CdS@NiCoP core-shell nanosphere for highly efficient visible-light-driven photocatalytic H_2 evolution. J Colloid Interface Sci, 2022, 608: 2730–2739

18 Li C, Du X, Jiang S, et al. Constructing direct Z-scheme heterostructure by enwrapping $ZnIn_2S_4$ on CdS hollow cube for efficient photocatalytic H_2 generation. Adv Sci, 2022, 9: 2201773
19 Lu X, Tong A, Luo D, et al. Confining single Pt atoms from Pt clusters on multi-armed CdS for enhanced photocatalytic hydrogen evolution. J Mater Chem A, 2022, 10: 4594–4600
20 Liu Y, Yang W, Chen Q, et al. Pt particle size affects both the charge separation and water reduction efficiencies of CdS-Pt nanorod photocatalysts for light driven H_2 generation. J Am Chem Soc, 2022, 144: 2705–2715
21 Li Z, Huang W, Liu J, et al. Embedding CdS@Au into ultrathin $Ti_{3-x}C_2T_y$ to build dual schottky barriers for photocatalytic H_2 production. ACS Catal, 2021, 11: 8510–8520
22 Zhao H, Wu M, Liu J, et al. Synergistic promotion of solar-driven H_2 generation by three-dimensionally ordered macroporous structured TiO_2-Au-CdS ternary photocatalyst. Appl Catal B-Environ, 2016, 184: 182–190
23 Ma X, Zhao K, Tang H, et al. New insight into the role of gold nanoparticles in Au@CdS core-shell nanostructures for hydrogen evolution. Small, 2014, 10: 4664–4670
24 Yu G, Wang X, Cao J, et al. Plasmonic Au nanoparticles embedding enhances the activity and stability of CdS for photocatalytic hydrogen evolution. Chem Commun, 2016, 52: 2394–2397
25 Luo M, Yao W, Huang C, et al. Shape effects of Pt nanoparticles on hydrogen production via Pt/CdS photocatalysts under visible light. J Mater Chem A, 2015, 3: 13884–13891
26 Ma L, Chen K, Nan F, et al. Improved hydrogen production of Au-Pt-CdS hetero-nanostructures by efficient plasmon-induced multipathway electron transfer. Adv Funct Mater, 2016, 26: 6076–6083
27 Zou J, Wu J, Wang Y, et al. Additive-mediated intercalation and surface modification of MXenes. Chem Soc Rev, 2022, 51: 2972–2990
28 Jiang J, Bai S, Yang M, et al. Strategic design and fabrication of MXenes-Ti_3CNCl_2@CoS_2 core-shell nanostructure for high-efficiency hydrogen evolution. Nano Res, 2022, 15: 5977–5986
29 Jiang J, Bai S, Zou J, et al. Improving stability of MXenes. Nano Res, 2022, 15: 6551–6567
30 Ran J, Gao G, Li F T, et al. Ti_3C_2 MXene co-catalyst on metal sulfide photo-absorbers for enhanced visible-light photocatalytic hydrogen production. Nat Commun, 2017, 8: 13907
31 Wang H, Hu P, Zhou J, et al. Ultrathin 2D/2D $Ti_3C_2T_x$/semiconductor dual-functional photocatalysts for simultaneous imine production and H_2 evolution. J Mater Chem A, 2021, 9: 19984–19993
32 Li Y H, Zhang F, Chen Y, et al. Photoredox-catalyzed biomass intermediate conversion integrated with H_2 production over $Ti_3C_2T_x$/CdS composites. Green Chem, 2020, 22: 163–169
33 Abbasi N M, Xiao Y, Zhang L, et al. Heterostructures of titanium-based MXenes in energy conversion and storage devices. J Mater Chem C, 2021, 9: 8395–8465
34 Li J, Wang H, Xiao X. Intercalation in two-dimensional transition metal carbides and nitrides (MXenes) toward electrochemical capacitor and beyond. Energy Environ Mater, 2020, 3: 306–322
35 Zou J, Zou Y, Wang H, et al. Tailoring the electronic acceptor-donor heterointerface between black phosphorus and Co_3O_4 for boosting oxygen bifunctional electrocatalysis. Chin Chem Lett, 2022, doi: 10.1016/j.cclet.2022.03.101
36 Zou J, Liao G, Wang H, et al. Controllable interface engineering of g-C_3N_4/CuS nanocomposite photocatalysts. J Alloys Compd, 2022, 911: 165020
37 Yin J, Zhan F, Jiao T, et al. Facile preparation of self-assembled MXene@Au@CdS nanocomposite with enhanced photocatalytic hydrogen production activity. Sci China Mater, 2020, 63: 2228–2238
38 Zuo G, Wang Y, Teo W L, et al. Ultrathin $ZnIn_2S_4$ nanosheets anchored on $Ti_3C_2T_x$ MXene for photocatalytic H_2 evolution. Angew Chem, 2020, 132: 11383–11388
39 Lee J T, Wyatt B C, Davis Jr. G A, et al. Covalent surface modification of $Ti_3C_2T_x$ MXene with chemically active polymeric ligands producing highly conductive and ordered microstructure films. ACS Nano, 2021, 15: 19600–19612
40 Zou J, Wu S, Liu Y, et al. An ultra-sensitive electrochemical sensor based on 2D g-C_3N_4/CuO nanocomposites for dopamine detection. Carbon, 2018, 130: 652–663
41 Liu W, Zheng Y, Zhang Z, et al. Ultrahigh gravimetric and volumetric capacitance in $Ti_3C_2T_x$ MXene negative electrode enabled by surface modification and *in-situ* intercalation. J Power Sources, 2022, 521: 230965
42 Feng R, Wan K, Sui X, et al. Anchoring single Pt atoms and black phosphorene dual co-catalysts on CdS nanospheres to boost visible-light photocatalytic H_2 evolution. Nano Today, 2021, 37: 101080
43 Lee S U, Jung H, Wi D H, et al. Metal-semiconductor yolk-shell heteronanostructures for plasmon-enhanced photocatalytic hydrogen evolution. J Mater Chem A, 2018, 6: 4068–4078
44 Zhao N, Hu Y, Du J, et al. $Ti_3C_2T_x$ MXene-derived amorphous TiO_2-C nanosheet cocatalysts coupled CdS nanostructures for enhanced photocatalytic hydrogen evolution. Appl Surf Sci, 2020, 530: 147247
45 Wang W, Hood Z D, Zhang X, et al. Construction of 2D $BiVO_4$-CdS-$Ti_3C_2T_x$ heterostructures for enhanced photo-redox activities. ChemCatChem, 2020, 12: 3496–3503
46 Yang Y, Zhang D, Xiang Q. Plasma-modified $Ti_3C_2T_x$/CdS hybrids with oxygen-containing groups for high-efficiency photocatalytic hydrogen production. Nanoscale, 2019, 11: 18797–18805
47 Dan M, Li J, Chen C, et al. MoS_2 and Ti_3C_2 ensembles into TiO_2 for efficient photocatalytic hydrogen evolution: Dual-bonding interactions and capacitive effect trigger the intrinsic activities. Energy Tech, 2022, 10: 2100188
48 Sun Y, Sun Y, Meng X, et al. Eosin Y-sensitized partially oxidized Ti_3C_2 MXene for photocatalytic hydrogen evolution. Catal Sci Technol, 2019, 9: 310–315
49 Xu F, Zhang D, Liao Y, et al. Synthesis and photocatalytic H_2-production activity of plasma-treated $Ti_3C_2T_x$ MXene modified graphitic carbon nitride. J Am Ceram Soc, 2020, 103: 849–858
50 Xi Y, Chen W, Dong W, et al. Engineering an interfacial facet of S-scheme heterojunction for improved photocatalytic hydrogen evolution by modulating the internal electric field. ACS Appl Mater Interfaces, 2021, 13: 39491–39500
51 Fu J, Xu Q, Low J, et al. Ultrathin 2D/2D WO_3/g-C_3N_4 step-scheme H_2-production photocatalyst. Appl Catal B-Environ, 2019, 243: 556–565
52 Jiang J, Ou-yang L, Zhu L, et al. Dependence of electronic structure of g-C_3N_4 on the layer number of its nanosheets: A study by Raman spectroscopy coupled with first-principles calculations. Carbon, 2014, 80: 213–221
53 Chen Y, Xie X, Xin X, et al. $Ti_3C_2T_x$-based three-dimensional hydrogel by a graphene oxide-assisted self-convergence process for enhanced photoredox catalysis. ACS Nano, 2018, 13: 295–304
54 Liu Y, Xiao H, Goddard Iii W A. Schottky-barrier-free contacts with two-dimensional semiconductors by surface-engineered MXenes. J Am Chem Soc, 2016, 138: 15853–15856